

Model-based clustering for spherical and hyper-spherical data using elliptically symmetric distributions

Theodoros Perdikis¹, Nader Alharbi², and Michail Tsagris ^{*3}

¹Department of Tourism Studies, University of Piraeus, Greece, theoperdik@unipi.gr

²King Saud bin Abdulaziz University for Health Sciences, and , King Abdullah
International Medical Research Center, Riyadh, Saudi Arabia,
alharbina@ksau-hs.edu.sa

³Department of Economics, University of Crete, Greece, mtsagris@uoc.gr

May 28, 2026

Abstract

Model-based clustering for directional data data has attracted a lot of interest, but most methods utilize rotationally symmetric distributions. This paper suggests the use of elliptically symmetric distributions, namely the elliptically symmetric angular Gaussian and the spherical elliptically symmetric projected Cauchy distributions that were recently proposed in the literature for modelling spherical data. The expectation-maximization algorithm is employed and the inclusion of covariates is also examined. Simulation studies compare the two distributions in terms of choosing the optimal number of clusters and computational cost. We use the mixtures of these two distributions to cluster two datasets on the sphere (earthquake locations) and two hyper-spherical datasets.

Keywords: spherical data, model-based clustering, elliptical symmetry

1 Introduction

Directional data refers to multivariate data constrained to a unit norm, with the sample space represented as:

$$\mathbb{S}^d = \left\{ \mathbf{x} \in \mathbb{R}^{d+1} \mid \|\mathbf{x}\| = 1 \right\},$$

*Corresponding author.

where $\|\cdot\|$ denotes the Euclidean norm. For $d = 1$, circular data reside on a circle, while for $d = 2$, spherical data are situated on a sphere. In this paper we focus on the case of spherical data. Such data are encountered in fields such as geology (Chang, 1986), environmental sciences (Heaton et al., 2014), image analysis (Straub et al., 2015), robotics (Bullock et al., 2014), and space (Kent et al., 2016), among others.

Numerous spherical (and hyper-spherical) distributions have been proposed over time, with the von Mises–Fisher (vMF) (Fisher, 1953) and projected normal (Kendall, 1974) distributions being among the earliest and most prevalent, while the spherical Cauchy (SC) (Kato and McCullagh, 2020) and Poisson kernel-based (PKB) distributions (Golzy and Markatou, 2020) are more recent propositions. However, these distributions assume rotational symmetry, which may restrict their applicability in certain scenarios.

To mitigate this constraint, Kent (1982) introduced an elliptically symmetric distribution that relaxes the rotational symmetry assumption. This distribution constitutes a special case of the Fisher–Bingham distribution (Mardia, 1975), and has proven valuable for modelling more sophisticated data structures. More recently, Paine et al. (2018) proposed the elliptically symmetric angular Gaussian (ESAG) distribution as an alternative to the Kent distribution, possessing some nice features (closed formula for the normalizing constant, straightforward random vector generation) and with contour lines that match closely those of Kent. ESAG emerges by projecting the Gaussian distribution onto the sphere and imposing two conditions on the covariance matrix in order to avoid indeterminacy. Moving along the same lines, Tsagris and Alzeley (2025) proposed the spherical elliptically symmetric projected Cauchy (SESPC) distribution, and Scealy and Wood (2019) proposed the scaled vMF, an elliptically symmetric distribution. These distributions, among others, have been applied to paleomagnetism (Scealy and Wood, 2019), geology (Dong and Melnykov, 2024), and in seismology to model earthquake data (Kagan, 2013, Kagan and Jackson, 2015, Walsh et al., 2009).

The focus of this paper is on model-based clustering with spherical and hyper-spherical data, or in other words, the problem of discovering latent groups (clusters) in possibly heterogeneous directional datasets. Under a model-based clustering point of view, we are modelling the observed data as a finite mixture of distributions. The Expectation–Maximization (EM) algorithm (Dempster et al., 1977) is a standard approach in estimating finite mixture models (Fruhworth-Schnatter et al., 2019, McLachlan, 2000, McNicholas, 2016, Yao and Xiang, 2024).

Banerjee et al. (2005), Hornik and Grün (2014) proposed mixtures of vMF distributions for clustering of directional data. Ever since, many works have dealt with this problem using mixtures of VMF distributions (Barbaro and Rossi, 2021, Gopal and Yang, 2014, McGraw et al., 2006, Røge et al., 2017, Taghia et al., 2014). Golzy and Markatou (2020) proposed mixtures of PKB distributions, and Tsagris et al. (2025) proposed mixtures of SC distributions. To the best of our knowledge, Peel et al. (2001) is the only paper that proposed model-based clustering using an elliptically symmetric distribution (the Kent distribution), and

more recently, [Dong and Melnykov \(2024\)](#) robustified the Kent mixtures model to account for outliers.

Let us visualize the effect of modelling spherical data via elliptical symmetric distributions in Figure 1. Suppose there are two known clusters of spherical data and we model each one of them using the vMF (rotationally symmetric) and the ESAG (elliptical symmetric) distributions. Evidently, in contrast to the two vMF distributions, the two ESAG distributions have fitted the two clusters adequately.

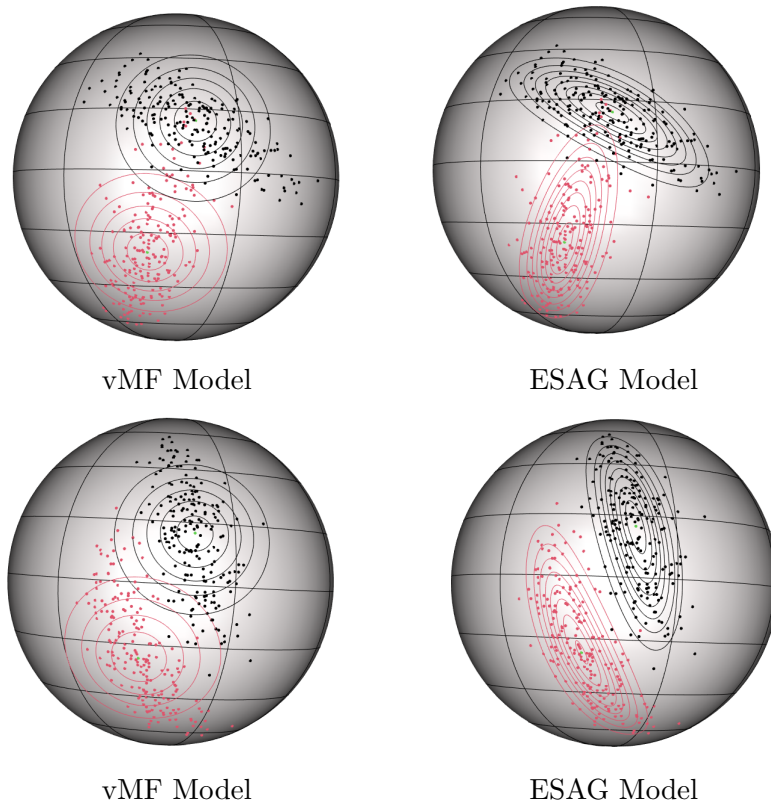


Figure 1: Contour plots for ESAG data: Modelled by the vMF (left column) and ESAG (right column).

In this paper, we propose model-based clustering using mixtures of ESAG and SESPC distributions for spherical and hyper-spherical data. We employ the EM algorithm to fit the mixtures with a fixed number of components K , and utilize the integrated completed likelihood (ICL) criterion ([Biernacki et al., 2000](#)) to choose the appropriate number of K . We compare, via simulation studies, the two distributions in terms of number of clusters, selected according to ICL, and quality of the clusters, measured by the adjusted Rand index (ARI), but also in terms of computational cost. When it comes to data that reside on the hyper-sphere we project them onto the sphere and then employ the same mixture models. We use these mixture models to cluster the locations of earthquake locations from two regions

(spherical), and wine quality and wholesales data (hyper-spherical).

The next section presents some preliminaries regarding the two distributions under study, while Section 3 explains the EM algorithm used to estimate the mixture models. Section 4 contains simulation studies offering an inter comparison of the two proposed mixture models and Section 5 illustrates their performance modelling the aforementioned (hyper-)spherical datasets. Finally, the Conclusions Section summarize the key findings of the paper.

2 Theoretical background of the distributions

2.1 The elliptically symmetric angular Gaussian distribution

Paine et al. (2018) proposed a new family of symmetrical distributions for spherical data. In fact, the ESAG distribution arises from projecting a multivariate normal on the sphere. Let \mathbf{X} be a d -dimensional random variable from a d -variate Normal distribution with covariance matrix \mathbf{V} and mean vector $\boldsymbol{\mu}$ which is projected on the circle/sphere/hyper-sphere, $\mathbf{Y} = \mathbf{X}/r$, where $r = \|\mathbf{X}\|$. The marginal distribution of \mathbf{Y} , denoted by angular Gaussian distribution (AG), arises by integrating out r

$$f(\mathbf{y}) = \int_0^\infty r^{d-1} f(r\mathbf{y}) dr, \quad (1)$$

resulting to

$$f_{\text{AG}}(\mathbf{y}) = \frac{C_d}{|\mathbf{V}|^{1/2} B^{d/2}} \exp \left[\frac{1}{2} \left(\frac{A^2}{B} - \Gamma^2 \right) \right] \mathcal{M}_{d-1} \left(\frac{B}{A^{1/2}} \right),$$

where $C_d = 1/(2\pi)^{(d-1)/2}$,

$$A = \mathbf{y}^\top \mathbf{V}^{-1} \boldsymbol{\mu}, \quad B = \mathbf{y}^\top \mathbf{V}^{-1} \mathbf{y}, \quad \text{and} \quad \Gamma^2 = \boldsymbol{\mu}^\top \mathbf{V}^{-1} \boldsymbol{\mu},$$

and, for real α ,

$$\mathcal{M}_{d-1}(\alpha) = \int_{u=0}^\infty u^{d-1} \frac{1}{(2\pi)^{1/2}} \exp \{ -(u - \alpha)^2 / 2 \} du.$$

Paine et al. (2018) showed that:

$$\mathcal{M}_0(\alpha) = \Phi(\alpha), \quad \mathcal{M}_1(\alpha) = \alpha\Phi(\alpha) + \phi(\alpha), \quad \mathcal{M}_2(\alpha) = (1 + \alpha^2)\Phi(\alpha) + \alpha\phi(\alpha),$$

where $\phi(\cdot)$ and $\Phi(\cdot)$ correspond to the p.d.f and c.d.f of the standard normal distribution, respectively. Paine et al. (2018) extended (1) into a general family, termed elliptically sym-

metric angular Gaussian distribution (ESAG), by imposing the following two conditions

$$\mathbf{V}\boldsymbol{\mu} = \boldsymbol{\mu}, \quad (2)$$

$$|\mathbf{V}| = 1. \quad (3)$$

As a result, it follows that the p.d.f. of the AG distribution presented in (1) can be expressed as:

$$f_{\text{ESAG}}(\mathbf{y}) = \frac{C_d}{B^{d/2}} \exp \left[\frac{1}{2} \left\{ \frac{(\mathbf{y}^\top \boldsymbol{\mu})^2}{B} - \boldsymbol{\mu}^\top \boldsymbol{\mu} \right\} \right] \mathcal{M}_{d-1} \left\{ \frac{\mathbf{y}^\top \boldsymbol{\mu}}{B^{1/2}} \right\}. \quad (4)$$

From (2), it can be seen that the positive definite matrix \mathbf{V} has a unit eigenvalue. By defining the other eigenvalues as

$$0 < \rho_1 \leq \dots \leq \rho_{d-1},$$

the inverse of covariance matrix \mathbf{V} can be written as:

$$\mathbf{V}^{-1} = \xi_d \xi_d^\top + \sum_{j=1}^{d-1} \xi_j \xi_j^\top / \rho_j,$$

where ξ_1, \dots, ξ_{d-1} and $\xi_d = \boldsymbol{\mu} / \|\boldsymbol{\mu}\|$ is a set of mutually orthogonal unit vectors and

$$\prod_{j=1}^{d-1} \rho_j = 1.$$

For $d = 3$, an efficient parametrization for the matrix \mathbf{V} which satisfies the constraints (2) and (3) and have two free parameters. More specifically, let $\tilde{\xi}_1$ and $\tilde{\xi}_2$ be two unit vectors orthogonal to each other and to the mean direction $\xi_3 = \boldsymbol{\mu} / \|\boldsymbol{\mu}\|$:

$$\tilde{\xi}_1 = (-\boldsymbol{\mu}_0^2, \mu_1 \mu_2, \mu_1 \mu_3)^\top / (\boldsymbol{\mu}_0 \|\boldsymbol{\mu}\|) \quad \text{and} \quad \tilde{\xi}_2 = (0, -\mu_3, \mu_2)^\top / \boldsymbol{\mu}_0,$$

where $\boldsymbol{\mu} = (\mu_1, \mu_2, \mu_3)^\top$ and $\boldsymbol{\mu}_0 = (\mu_2^2 + \mu_3^2)^{1/2}$. Additionally, the axes of symmetry ξ_1 and ξ_2 are expressed as:

$$\xi_1 = \cos \psi \tilde{\xi}_1 + \sin \psi \tilde{\xi}_2 \quad \text{and} \quad \xi_2 = -\sin \psi \tilde{\xi}_1 + \cos \psi \tilde{\xi}_2,$$

where $\psi \in (0, \pi]$ is the angle of rotation. Finally, by defining the pair $\boldsymbol{\gamma} = (\gamma_1, \gamma_2)^\top$ as

$$\gamma_1 = 2^{-1}(\rho^{-1} - \rho) \cos 2\psi \quad \text{and} \quad \gamma_2 = 2^{-1}(\rho^{-1} - \rho) \sin 2\psi,$$

where $\rho_1 = \rho$ and $\rho_2 = 1/\rho$ for $\rho \in (0, 1]$, \mathbf{V}^{-1} can be expressed as:

$$\mathbf{V}^{-1} = \mathbf{I}_3 + \gamma_1 \left(\tilde{\xi}_1 \tilde{\xi}_1^\top - \tilde{\xi}_2 \tilde{\xi}_2^\top \right) + \gamma_2 \left(\tilde{\xi}_1 \tilde{\xi}_2^\top + \tilde{\xi}_2 \tilde{\xi}_1^\top \right) + \left\{ (\gamma_1^2 + \gamma_2^2 + 1)^{1/2} - 1 \right\} \left(\tilde{\xi}_1 \tilde{\xi}_1^\top + \tilde{\xi}_2 \tilde{\xi}_2^\top \right),$$

where \mathbf{I}_3 denotes the 3-dimensional identity matrix.

2.2 The spherical elliptically symmetric projected Cauchy distribution

Tsagris and Alzeley (2025) projected the 3-dimensional Cauchy distribution on the sphere and, by imposing the same conditions as in ESAG (2)–(3), introduced the spherical elliptically symmetric projected Cauchy distribution (SESPC) as:

$$f_{\text{SESPC}}(\mathbf{y}) = \frac{B (\|\boldsymbol{\mu}\|^2 + 1) \sqrt{E} \left[\arctan 2 \left(\sqrt{E}, -\mathbf{y}^\top \boldsymbol{\mu} \right) - \arctan 2 \left(\sqrt{E}, \mathbf{y}^\top \boldsymbol{\mu} \right) + \pi \right] + 2 \mathbf{y}^\top \boldsymbol{\mu} E}{4\pi^2 B E^2},$$

where $E = B\|\boldsymbol{\mu}\|^2 + B - (\mathbf{y}^\top \boldsymbol{\mu})^2$ and $\arctan 2$ is the 2-argument arc tangent. Similarly to the design of the ESAG distribution the corresponding inverse of the covariance matrix of \mathbf{y} , \mathbf{V} is computed in the same exact manner.

3 Model-based clustering

Let K be the number of clusters of a population where p_1, \dots, p_K are the clusters' unknown weights where $p_j > 0$ and $\sum_{j=1}^K p_j = 1$. Furthermore, we shall denote $\mathbf{Z}_i = (Z_{i1}, \dots, Z_{in})^\top$, $i = 1, \dots, n$ as the latent allocation variables following the multinomial distribution, $\mathbf{Z}_i \sim \mathcal{M}(1; p_1, \dots, p_K)$, with K categories and success probabilities equal to p_1, \dots, p_K which are the corresponding prior probabilities of selecting an observation from cluster j . The distribution of \mathbf{Y}_i conditionally on $\mathbf{Z}_i = \mathbf{z}_i$, can be expressed as:

$$\mathbf{Y}_i | (\mathbf{Z}_i = \mathbf{z}_i) \sim f_{\mathbf{Y}_i | \mathbf{Z}_i}(\mathbf{y}_i | \mathbf{z}_i) = \prod_{j=1}^K f^{z_{ij}}(\mathbf{y}_i; \boldsymbol{\mu}_j, \gamma_j), \quad \text{independent for } i = 1, \dots, n \quad (5)$$

where $f(\cdot; \boldsymbol{\mu}_j, \gamma_j)$ denotes the probability density function of the 3-dimensional ESPC or ESAG distribution with parameter $\boldsymbol{\mu}_j, \gamma_j$ for $j = 1, \dots, K$. When $Z_{ij} = 1$ i.e. the j -th element of \mathbf{Z}_i is equal to 1, the above equation can be written as $\mathbf{Y}_i | (Z_{ij} = 1) \sim f(\cdot; \boldsymbol{\mu}_j)$. Additionally, the joint distribution of $\mathbf{Y}_i, \mathbf{Z}_i$ is

$$(\mathbf{Y}_i, \mathbf{Z}_i) \sim f_{\mathbf{Y}_i, \mathbf{Z}_i}(\mathbf{y}_i, \mathbf{z}_i) = \prod_{j=1}^K \{p_j f(\mathbf{y}_i; \boldsymbol{\mu}_j, \gamma_j)\}^{z_{ij}}. \quad (6)$$

while the marginal distribution of \mathbf{Y}_i is expressed as a mixture of K distributions

$$\mathbf{Y}_i \sim f_{\mathbf{Y}_i}(\mathbf{y}_i) = \sum_{j=1}^K p_j f(\mathbf{y}_i; \boldsymbol{\mu}_j, \gamma_j), \quad \text{independent for } i = 1, \dots, n. \quad (7)$$

Furthermore, the conditional probability that an observation i is assigned to component j , given that $\mathbf{Y}_i = \mathbf{y}_i$, equals to

$$P(Z_{ij} = 1 | \mathbf{Y}_i = \mathbf{y}_i) = \frac{p_j f(\mathbf{y}_i; \boldsymbol{\mu}_j, \gamma_j)}{\sum_{\ell=1}^K p_\ell f(\mathbf{y}_i; \boldsymbol{\mu}_\ell, \gamma_\ell)} =: w_{ij}, \quad j = 1, \dots, K \quad (8)$$

or equivalently, $\mathbf{Z}_i | (\mathbf{Y}_i = \mathbf{y}_i) \sim \mathcal{M}(1, w_{i1}, \dots, w_{iK})$, independent for $i = 1, \dots, n$.

Finally, the observed log-likelihood is defined as

$$\ell(\boldsymbol{\mu}, \boldsymbol{\gamma}, \mathbf{p} | \mathbf{y}) = \sum_{i=1}^n \log \left\{ \sum_{j=1}^K p_j f(\mathbf{y}_i; \boldsymbol{\mu}_j, \gamma_j) \right\}, \quad (9)$$

where $\boldsymbol{\mu}, \boldsymbol{\gamma} \in \mathbb{R}^{4K}$, $\mathbf{p} \in \mathcal{P}_{K-1}$, where $\mathcal{P}_{K-1} = \{p_1, \dots, p_K : p_j > 0, j = 1, \dots, K, \sum_{j=1}^K p_j = 1\}$. It is clear the fact that the scope is to maximize (9). In order to achieve that, similarly with the work of [Tsagris et al. \(2025\)](#), the EM algorithm is been considered where for a set of starting values, the expectation of the complete log-likelihood (E-step) is computed and then is maximized with respect to $\boldsymbol{\mu}, \mathbf{p}$ and $\boldsymbol{\gamma}$. (M-step). In particular, the complete log-likelihood, is

$$\ell_c(\boldsymbol{\mu}, \boldsymbol{\gamma}, \mathbf{p} | \mathbf{y}, \mathbf{z}) = \sum_{i=1}^n \sum_{j=1}^K z_{ij} [\log p_j + \log f(\mathbf{y}_i; \boldsymbol{\mu}_j, \gamma_j)]. \quad (10)$$

E-step. At iteration t , given the current parameter estimates $\Theta^{(t)} = \{\boldsymbol{\mu}^{(t)}, \boldsymbol{\gamma}^{(t)}, \mathbf{p}^{(t)}\}$, the expected value of Z_{ij} is computed with respect to the conditional distribution $Z_i | (Y_i = \mathbf{y}_i, \Theta^{(t)})$. The corresponding membership probabilities are derived as:

$$w_{ij}^{(t)} = \frac{p_j^{(t)} f(\mathbf{y}_i; \boldsymbol{\mu}_j^{(t)}, \gamma_j^{(t)})}{\sum_{\ell=1}^K p_\ell^{(t)} f(\mathbf{y}_i; \boldsymbol{\mu}_\ell^{(t)}, \gamma_\ell^{(t)})}, \quad i = 1, \dots, n, \quad j = 1, \dots, K. \quad (11)$$

M-step. At this step, the expected complete log-likelihood $Q(\Theta | \Theta^{(t)}) = \mathbb{E}[\ell_c | \mathbf{y}, \Theta^{(t)}]$ is maximised with respect to Θ and the mixing proportions are updated as the weighted averages of the posterior probabilities:

$$p_j^{(t+1)} = \frac{1}{n} \sum_{i=1}^n w_{ij}^{(t)}, \quad j = 1, \dots, K. \quad (12)$$

Due to the fact that neither the ESAG nor the SESPC density yields a closed-form maximizer for (μ_j, γ_j) , the weighted log-likelihood contribution of component j ,

$$Q_j(\mu_j, \gamma_j) = \sum_{i=1}^n w_{ij}^{(t)} \log f(y_i; \mu_j, \gamma_j), \quad (13)$$

is maximized numerically. Specifically, for each component $j = 1, \dots, K$, a general-purpose optimizer (e.g. Nelder-Mead) is applied to $-Q_j$, and the procedure is restarted until the improvement in the objective falls below 10^{-5} , yielding the updated estimates $\mu_j^{(t+1)}$ and $\gamma_j^{(t+1)}$.

Regarding the optimal number of clusters the integrated complete likelihood (ICL) has been considered (Biernacki et al. (2003)). Initialization of the EM algorithm demands extra care in order to avoid convergence to local maxima. Some indicative works on this topic include Baudry and Celeux (2015), Biernacki et al. (2003), Fraley et al. (2005), Karlis and Xekalaki (2003), Michael and Melnykov (2016), Papastamoulis et al. (2016). In our implementation of the mixtures of ESAG and SESPC distributions, we tried two initialization schemes. One based on k -means starting values and one based on Gaussian mixture models (GMMs). The first strategy is adequate for rotationally symmetric distributions (Tsagris et al., 2025), but in our case GMMs that allow for a structured covariance was shown to yield better performance.

3.1 Inclusion of covariates

We may link the mixing probabilities p_j to some covariates \mathbf{X} yielding the concomitant model

$$p_j(\mathbf{x}_i) = \frac{\exp(\mathbf{x}_i^\top \boldsymbol{\beta}_j)}{\sum_{\ell=1}^K \exp(\mathbf{x}_i^\top \boldsymbol{\beta}_\ell)}. \quad (14)$$

In this case we substitute the p_j in Eq (12) with $p_j(\mathbf{x}_i)$ from Eq. (14), and hence the M-step requires an extra optimization. The $\boldsymbol{\beta}_{js}$ are obtained from maximization of the following quantity

$$D_j = \sum_{i=1}^{n_j} w_{ij}^{(t)} \log [p_j(\mathbf{x}_i)], \quad j = 1, \dots, K.$$

The maximization of D_j is performed independently of the maximization of the weighted log-likelihood in Eq. (13), and the observed log-likelihood (9) now becomes

$$\ell(\boldsymbol{\mu}, \boldsymbol{\gamma}, \mathbf{p} | \mathbf{y}) = \sum_{i=1}^n \log \left\{ \sum_{j=1}^K p_j(\mathbf{x}_i) f(\mathbf{y}_i; \boldsymbol{\mu}_j, \gamma_j) \right\}.$$

We may also link the mean vector of the ESAG or SESPC to some covariates yielding the mixtures of regressions model, where $\boldsymbol{\mu}_j(\mathbf{x}_i) = \mathbf{x}_i^\top \boldsymbol{\beta}_j$. In this case, the observed log-likelihood

becomes

$$\ell(\boldsymbol{\mu}, \boldsymbol{\gamma}, \mathbf{p}|\mathbf{y}) = \sum_{i=1}^n \log \left\{ \sum_{j=1}^K p_j f(\mathbf{y}_i; \boldsymbol{\mu}_j (\mathbf{x}_i^\top \boldsymbol{\beta}_j), \gamma_j) \right\}.$$

Both the ESAG and the SESPC offer the possibility to relate their γ parameters to some covariates in the same linear manner, at the cost of increased computational cost. The last option is to add the covariates in both the mixing probabilities and the parameters of either distribution, but this is computationally expensive.

3.2 Visual inspection of the mixtures of ESAG and SESPC distributions

Our scope is to investigate the performance of each model assuming two scenarios where the data comes from the ESAG distribution and the data comes from the SESPC distribution. For each case, under the assumption that the true number of cluster is two, we will compare the performance of each model using simulation based on their corresponding ARI value. Before we proceed to any numerical investigations, it is important to investigate the effect on the vector parameter γ on forming a cluster. Regarding the structure of the clusters, the same fixed values of mean vectors are used. In particular, for a given mean vector $\boldsymbol{\mu}_1$, using the corresponding unit vector $\boldsymbol{\mu}'_1 = \frac{\boldsymbol{\mu}_1}{\|\boldsymbol{\mu}_1\|}$, we find a vector $\boldsymbol{\mu}'_2$ such that the angle between $\boldsymbol{\mu}'_1$ and $\boldsymbol{\mu}'_2$ is equal to ω . Lastly, we simulate a dataset forming two cluster by generating a random sample of size $n = 200$ from of a mixture of ESAG (SESPC) distributions with approximately equal mixing probabilities, $p_1 \approx p_2$. For each cluster the corresponding mean vectors are considered to be equal to $\tau_1 \times \boldsymbol{\mu}'_1$ and $\tau_2 \times \boldsymbol{\mu}'_2$ respectively. Note that, the values of $\boldsymbol{\tau} = (\tau_1, \tau_2)$ play the role of the consecration parameter.

In Figure 2 the corresponding shape of two clusters is presented under different values of γ . For all the cases of γ as illustrated in Figure 2 we set $\omega = 45$, $\boldsymbol{\mu}'_1 = (-0.927, -0.282, 0.249)$ where $\boldsymbol{\mu}_1$ was generated based on three random numbers from $N(0, 1)$ and $\boldsymbol{\mu}'_2 = (-0.886, -0.008, -0.464)$ was the same value for all the cases. For illustration purposes we fix the values of (τ_1, τ_2) at $(5, 5)$. As it will be shown hereafter, the values of (τ_1, τ_2) play the role of the consecration parameter. From Figure 2 it can be seen how the values of γ affect on how these clusters are formed. Note that, we intentionally considered these specific valued of γ in order to investigate each model's performance under the scenarios where the two clusters are formed vertically or in an angle. Additionally, it can be observed that, considering exact the same parameters for both distribution, the SESPC distribution is more spread that the ESAG but the corresponding relation between the two clusters remains the same.

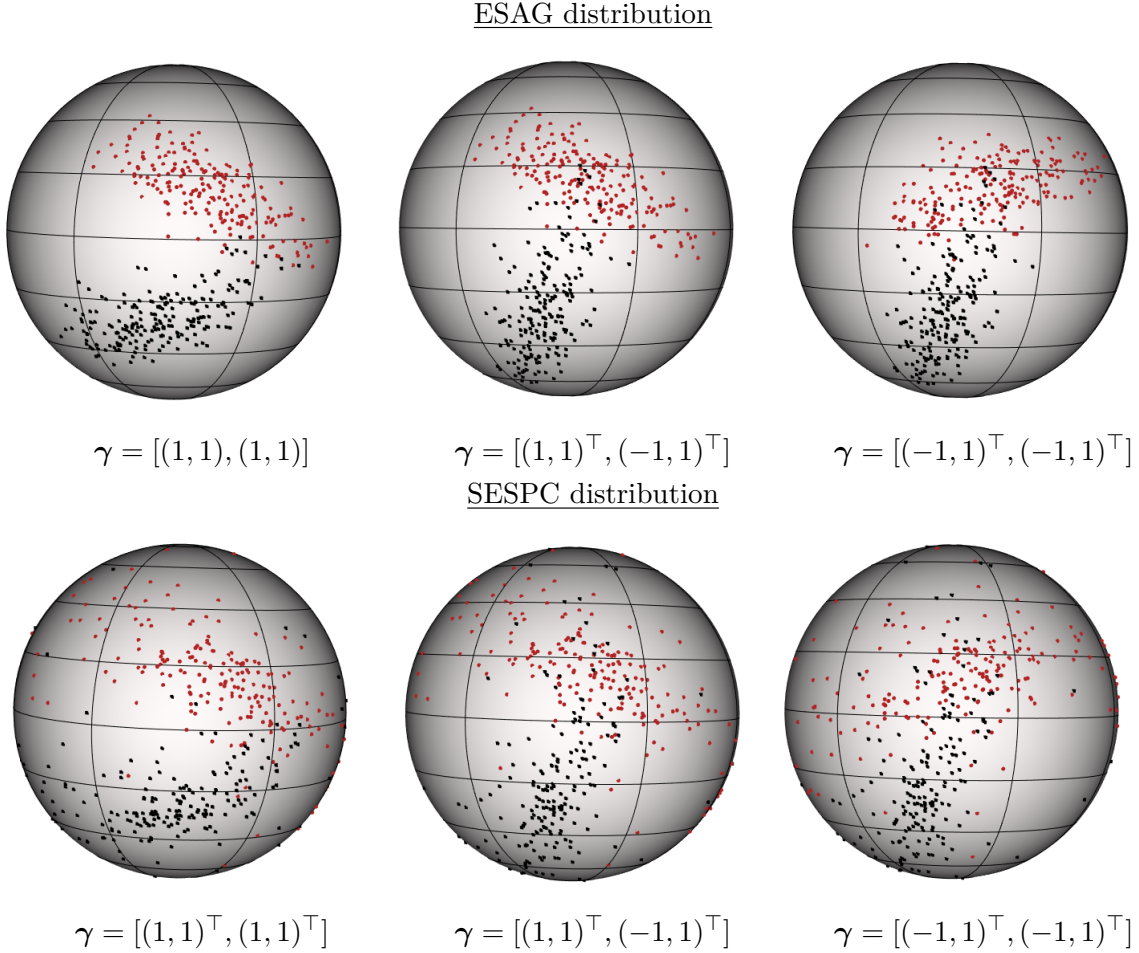


Figure 2: Effect of γ for ESAG distribution (top row, with $(\tau_1, \tau_2) = (5, 5)$) and SESPC distribution (bottom row, with $(\tau_1, \tau_2) = (5, 5)$). For all cases, $\boldsymbol{\mu}'_1 = (-0.927, -0.282, 0.249)^\top$, $\boldsymbol{\mu}'_2 = (-0.886, -0.008, -0.464)^\top$.

3.3 Model-based clustering with hyper-spherical data

The drawback of the SESPC is that, unlike the ESAG which was proposed for arbitrary dimensions, the SESPC was developed for spherical data. [Zehao and Xianzheng \(2024\)](#) proposed a novel parameterization of the ESAG distribution for hyper-spherical data and we used it in the EM algorithm. The computational cost of the EM is high and for this reason we suggest to project the data onto the sphere using principal geodesic analysis-based sphere projection ([Fletcher et al., 2004](#), [Jung et al., 2012](#)) and then apply the SESPC or ESAG mixture model. In Figure 3 several Sphere plot are illustrated of the projected 10-dimensional data into the sphere. The corresponding parameter γ_1 , γ_2 and $\boldsymbol{\mu}_1, \boldsymbol{\mu}_2$ are presented in Table in Appendix.

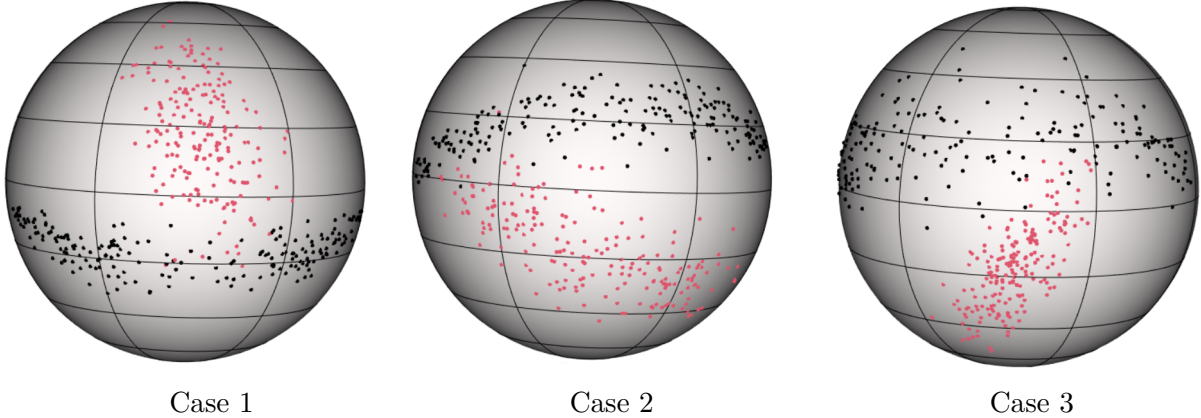


Figure 3: Hyper-spherical data for the 10-dimensional ESAG distribution. The values of γ_1, γ_2 and μ_1, μ_2 are presented in Table in Appendix

4 Simulation studies

4.1 Numerical analysis for Spherical data

Firstly, the performance of each method, assuming almost equal sizes for the two clusters, is investigated (total size $n = 200$). In Figure 4 the performance of the two models are presented. In particular, for $R = 50$ iterations (i.e simulating 50 different samples consisting of two clusters) the boxplots of the the Adjusted Rand index (ARI) metric are presented. For simplicity, in the results presented below we shall denote as ARI^{ESAG} (ARI^{SEPC}) the ARI values obtained considering the ESAG (SEPC) model. We may see that:

- ESAG distribution: When the model being considered is the ESAG, it can create the correct number of clusters in all the cases where large values of ARI indicate the correct number of predicted clusters. Additionally, when the model is the SEPC, the performance does not significantly change. In particular, for the case where $\gamma = [(1, 1)^\top, (1, 1)^\top]$ ($\gamma = [(1, 1)^\top, (-1, 1)^\top]$), the boxplots of ARI^{ESAG} 's are narrowed comparing to the boxplots of ARI^{SEPC} with corresponding medians close to 0.9 (0.85). Lastly, when $\gamma = [(-1, 1)^\top, (-1, 1)^\top]$ the boxplots of ARI^{ESAG} 's are wider comparing to the boxplots of ARI^{SEPC} with corresponding medians close to 0.8. In summary, for all the investigated scenarios, both models can detect the correct number of clusters and give similar ARI values larger than 0.8 while the worst performance is achieved under the third case.
- SEPC distribution: Using the SEPC model can effectively define the correct number of clusters in most of the cases. Furthermore, for all the cases, the boxplots of ARI^{SEPC} do not significantly differ. On the other hand, using the ESAG model the efficiency on

detecting the correct number of clusters is worse and the boxplots of ARI^{ESAG} are smaller. .

- Performance comparisons: The performance of each model is better when the data comes from the ESAG distribution, which is an expected results since in both cases the same values of $\tau = (5, 5)$ are considered and the ESPC is more spread in the tails compared to the ESAG distribution. This can be visually justified by looking at Figure 2.

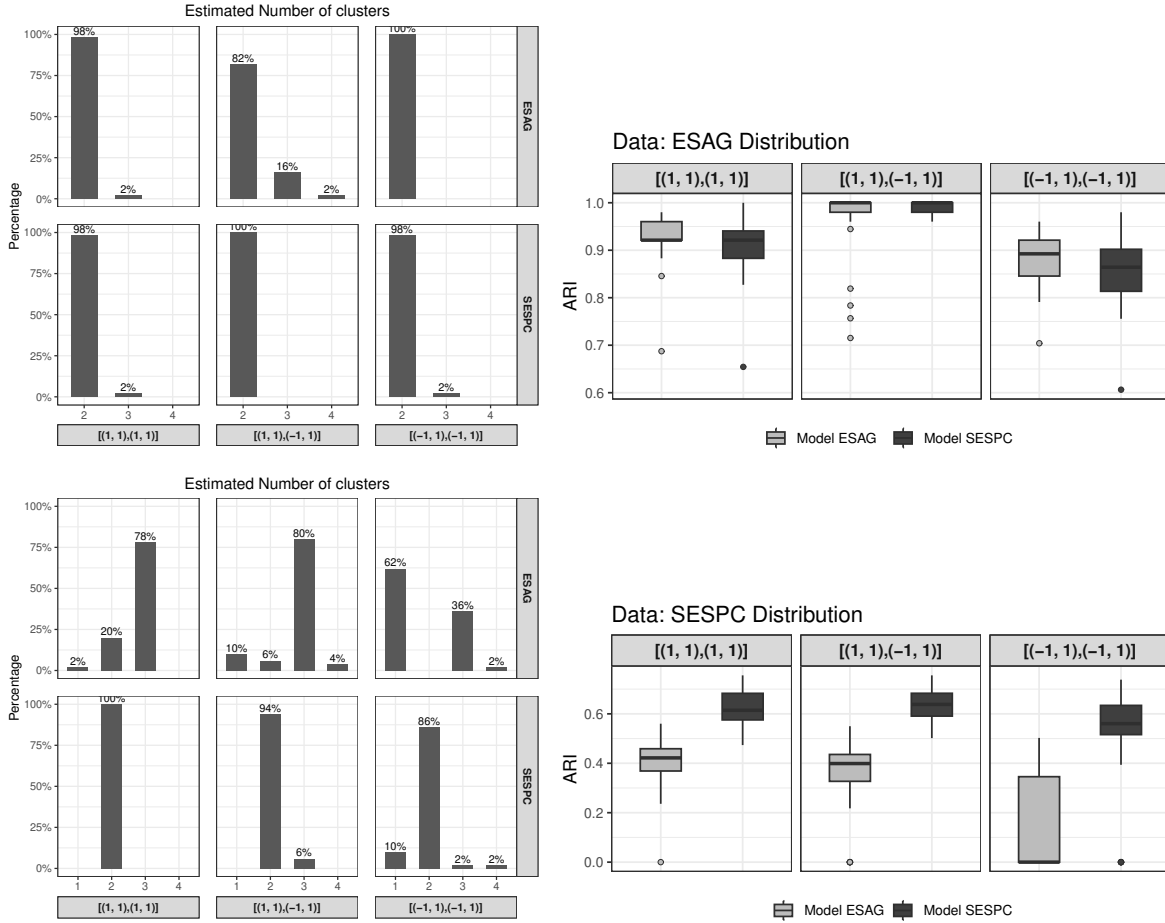


Figure 4: ESAG and SESPC generated data with equal clusters: $n = 200$, $\omega = 45^\circ$, $\mu'_1 = (-0.927, -0.282, 0.249)^\top$, $\mu'_2 = (-0.886, -0.008, -0.464)^\top$, $(\tau_1, \tau_2) = (5, 5)$, and various γ combinations.

In Figure 5 some additional performance comparisons between the two models are illustrated but now the probabilities of an observation to belong in a cluster is randomly generated from the 2-dimensional Dirichlet distribution. Note that, we intentionally increase the number of iteration on $R = 100$ in order to capture many scenarios with respect to the size of

each cluster. More specifically, it can be observed that:

- ESAG distribution: When the model being considered is the ESAG, it can create the correct number of clusters in almost all the cases the boxplots of ARI^{SEPC} do not significantly differ. On the other hand, when the model is the SESPC, the performance does not significantly change for the first two cases while for the third one the variability of ARI^{SEPC} is very large.
- SESPC distribution: The SESPC model can effectively define the correct number of clusters in most of the cases. Furthermore, for all the cases, the the boxplots of ARI^{SEPC} do not significantly change. On the other hand, using the ESAG model the efficiency on detecting the correct number of clusters is worse and the boxplots of ARI^{ESAG} are smaller.
- Performance comparisons: The performance of each model is better when the data comes from the ESAG distribution, which is an expected results since in both cases the same values of $\tau = (5, 5)$ are considered and the ESPC is more spread in the tails compared to the ESAG distribution. This can be visually justified by looking at [Figure 2](#).

It can be seen that the results regarding the performance between the two models is more or less the same. The difference is that when the data come from the SESPC distribution the performance of the ESAG model is worse.

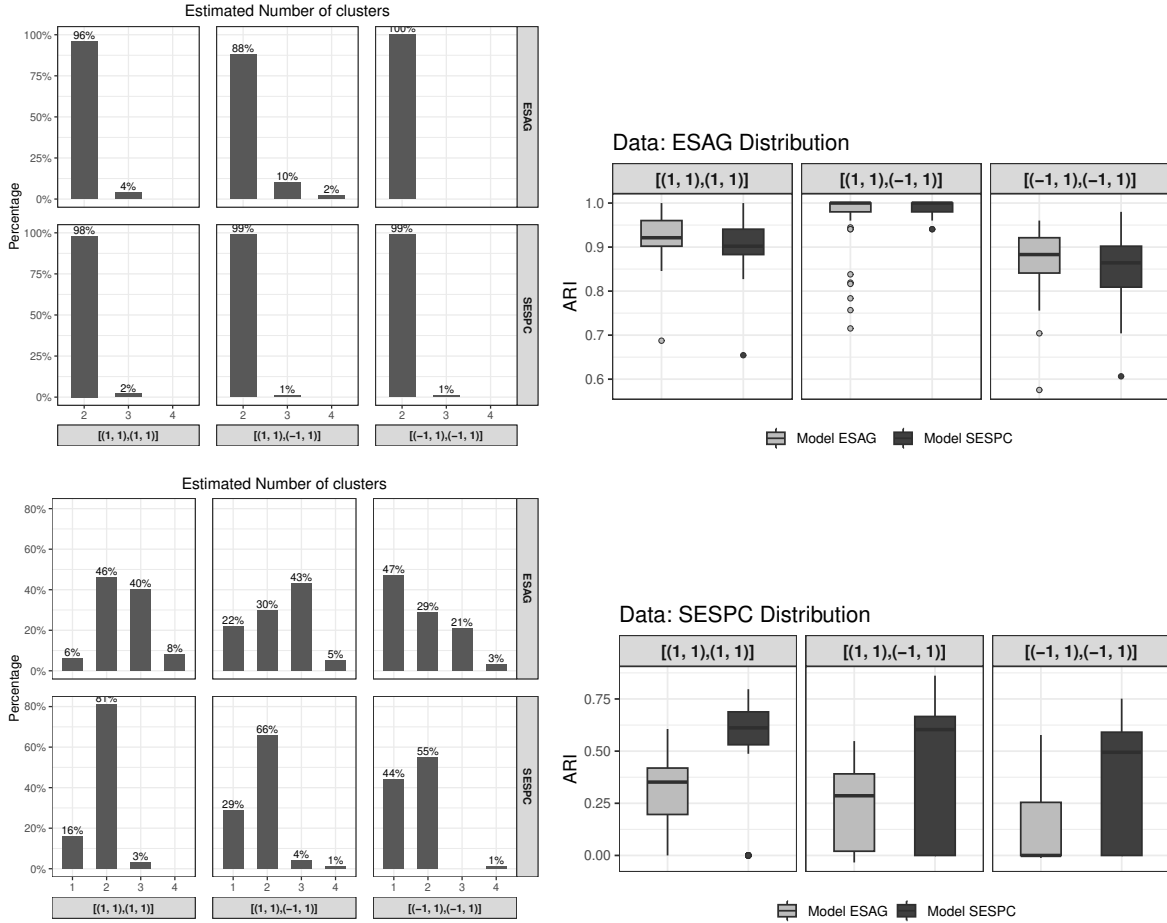


Figure 5: ESAG and SESPC generated data with unequal clusters: $n = 200$, $\omega = 45^\circ$, $\mu'_1 = (-0.927, -0.282, 0.249)^\top$, $\mu'_2 = (-0.886, -0.008, -0.464)^\top$, $(\tau_1, \tau_2) = (5, 5)$, and various γ combinations.

In Figure 6 the effect of sample size in the performance of each model is investigated for $n = \{100, 200, 500\}$. Without loss of generality we assume that, for each case, the probabilities for an observation to belong at each cluster are the same. It can be seen that, for each model and investigated scenario, as the size of the sample size increases, the model's performance is improved resulting in higher and narrowed boxplots of the ARI values. Additional results are presented in Figure 7 regarding the effect of the concentration parameter τ . As it was previously highlighted, small (large) values of τ_1 , τ_2 result in small (large) spread in the corresponding clusters. This, as expected, affects the models' performance. In particular for small combination of $(\tau_1, \tau_2) = (2, 2)$ both models do not perform well since are not able to detect the correct number of cluster in most of the cases. As the magnitude of the concentration increases the performance of each models is improved.

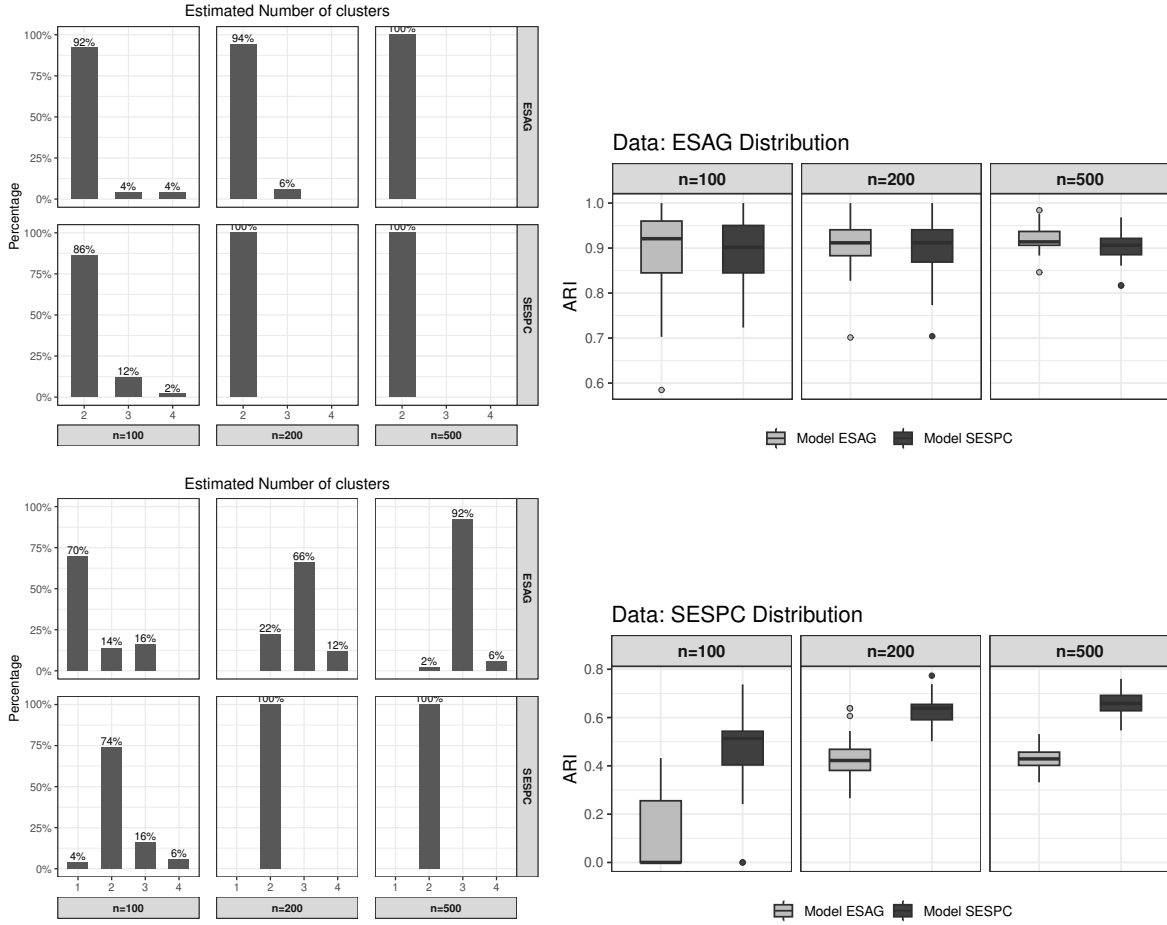


Figure 6: ESAG and SESPC generated data with equal clusters: effect of n . $\gamma = [(1, 1)^\top, (1, 1)^\top]$, $\omega = 45^\circ$, $\mu'_1 = (-0.927, -0.282, 0.243)^\top$, $\mu'_2 = (-0.886, -0.008, -0.464)^\top$ and $(\tau_1, \tau_2) = [(2, 2), (4, 4), (5, 5), (5, 10)]$.

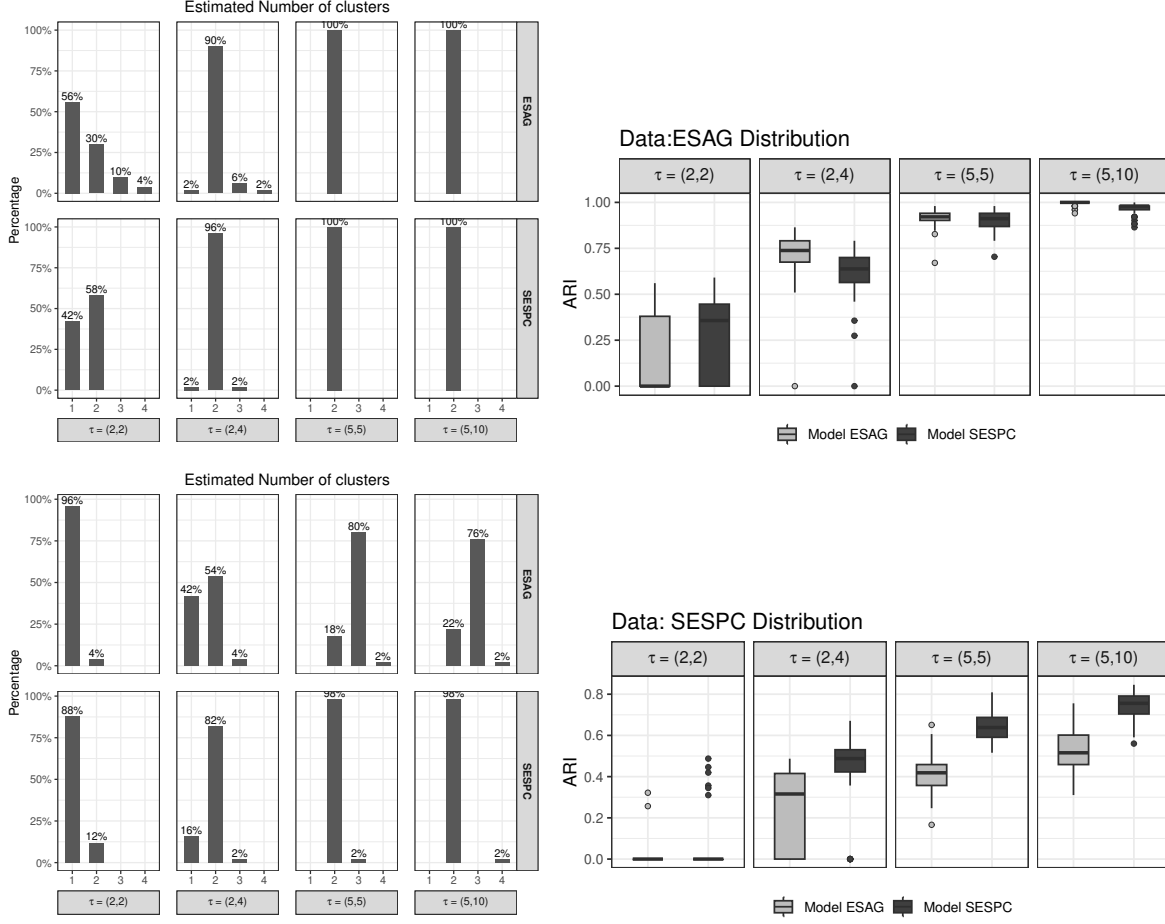


Figure 7: ESAG and SESPC generated data with equal clusters: effect of $\tau.n = 200$, $\gamma = [(1, 1)^\top, (1, 1)^\top]$, $\omega = 45^\circ$, $\mu'_1 = (-0.927, -0.282, 0.243)^\top$, $\mu'_2 = (-0.886, -0.008, -0.464)^\top$ and $(\tau_1, \tau_2) = [(2, 2), (4, 4), (5, 5), (5, 10)]$.

4.2 Numerical analysis for hyper-spherical data

In the remainder of this section the performance of the ESAG and SESPC models is investigated for hyper-spherical data of dimension $d = 10$ considering the cases presented in Figure 3. In particular our scope is to investigate the effect of the sample size, the size of each cluster and how the clusters are formed in the performance of each model. In Figure 3, similarly to the previous Section where $d = 3$, we assume equal probabilities for each cluster under the case 1. It can be seen that, for $n = 500$, both models have similar performance. Additionally, for $n = \{100, 200\}$ the boxplots of the ARI values corresponding to the SESPC model have smaller variability and lies inside the the boxplots which corresponds to the ESAG model. Lastly, the boxplots of ARI's regarding the performance of each model is presented under the assumption of have equal (9) and unequal (10) cluster. In both Figures, we may observe that the relation between the performance of each model is more is less the same, with the

difference that when having unequal clusters, as expected, the width of the boxlots is slightly larger.

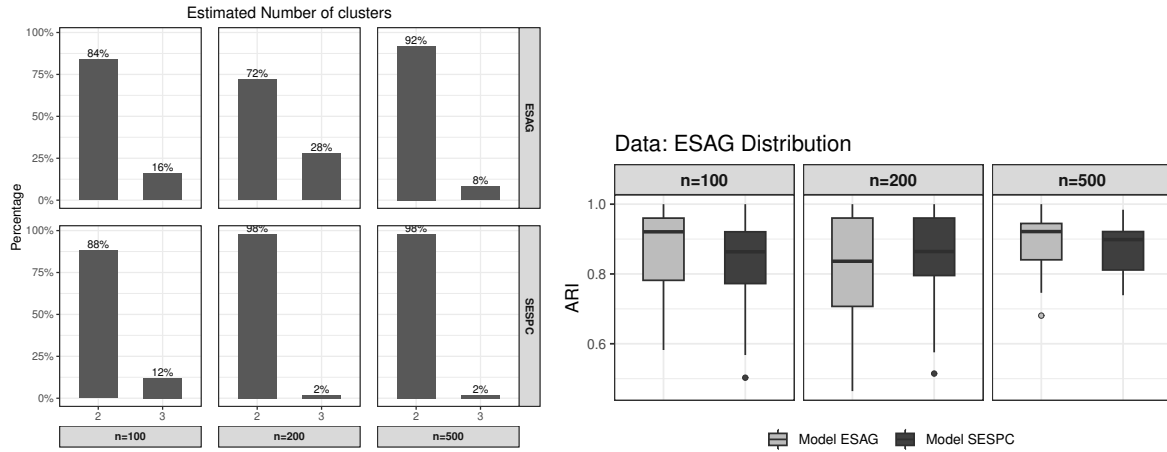


Figure 8: Hyper-spherical ESAG generated data with equal clusters: effect of n . $\omega = 45^\circ$, The values of γ_1 , γ_2 and μ_1, μ_2 are presented in the Appendix.

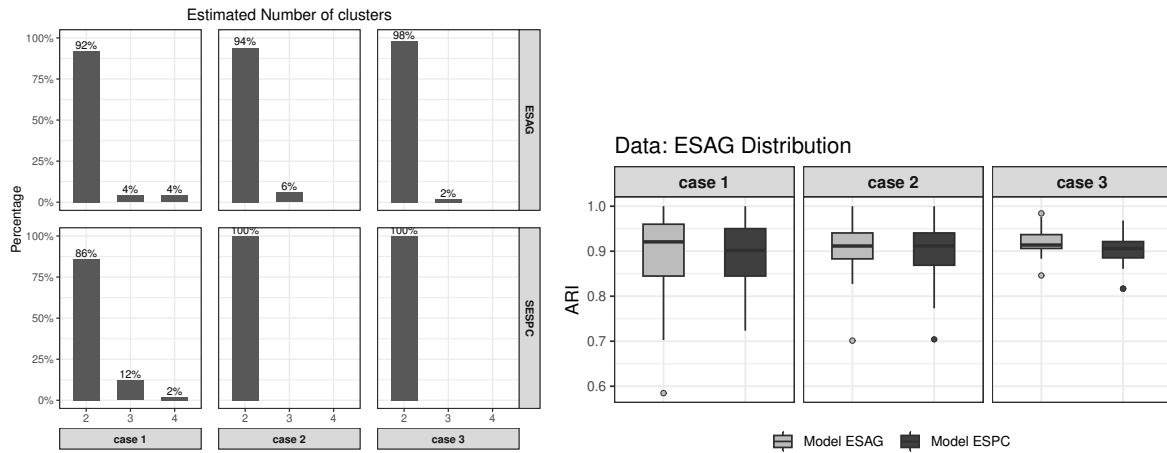


Figure 9: Hyper-spherical ESAG generated data with equal clusters: $n = 200$, $\omega = 45^\circ$, The values of γ_1 , γ_2 and μ_1, μ_2 are presented in the Appendix.

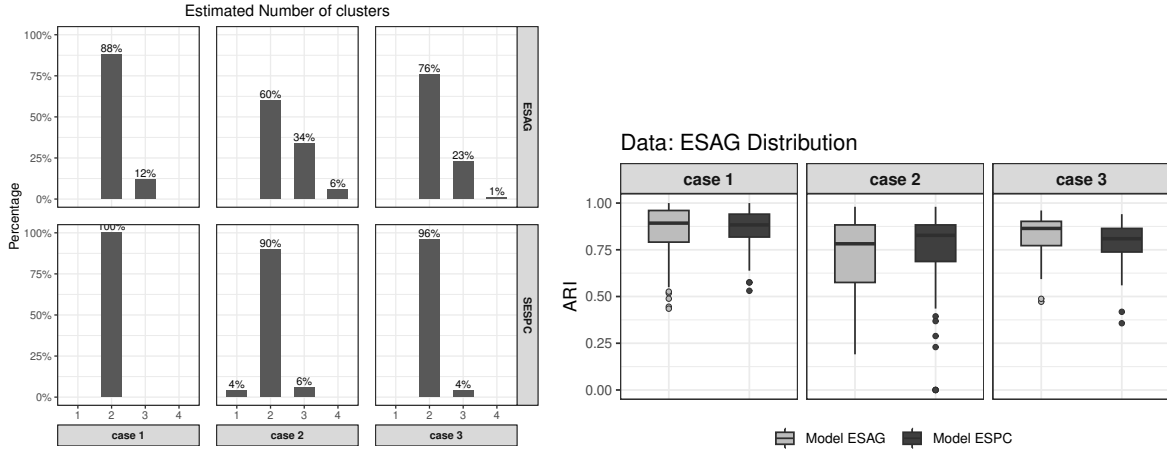


Figure 10: Hyper-spherical ESAG generated data with unequal clusters: $n = 200$, $\omega = 45^\circ$, The values of γ_1 , γ_2 and μ_1, μ_2 are presented in the Appendix.

4.3 Computational cost

Figure 11 presents the computational cost for each model as a function of the sample size $n = 200, 500, 1000$. In particular, for each model, 10 iterations were considered and the required time (in seconds) to obtain the results, searching for $K = 1, \dots, 4$ clusters, was computed by using a computer with Intel(R) Core(TM) i7-8550U CPU with 16 GB RAM without performing parallel computing (an option which is available for these computations). The box-plots of time are presented in Figure 11. It can be seen that, as expected, as the sample size increases the computational time also increases in both cases. Comparing the two models, it is evident that, regardless of the sample size, the SESPC model is faster.

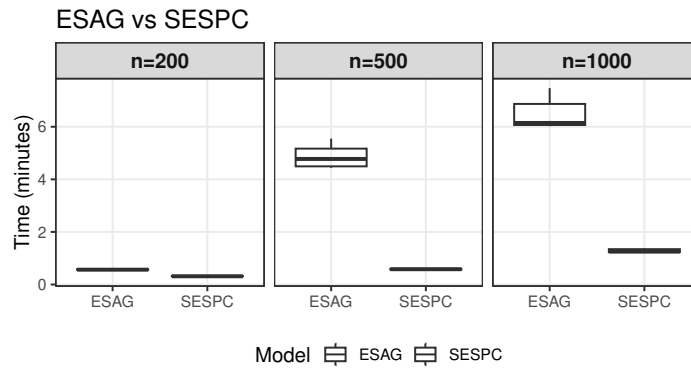


Figure 11: Box-plots of ESAG vs SESPC computational cost of searching for the optimal number of clusters.

5 Real data analysis

We illustrate the performance of the SESPC and ESAG mixture models using four real datasets. The first two datasets contain locations of the earthquakes that took place (a) in the North American continent during 1900 and 2025¹ and (b) in a cube near Fiji since 1964². For North America we collected the earthquakes whose magnitude was 5 or higher in the Richter scale, whereas for the Fiji region the magnitude of the earthquakes was of 4 Richter or higher. North America contributes with 366 locations from Canada, Dominican Republic, Guatemala, Haiti, Jamaica, Mexico, and USA, with the last two countries containing the 87.43% of the observations. The Fiji region consists of 1,000 locations from New Zealand, Solomon Islands and Vanuatu, but the vast majority (98.3%) refers to earthquakes that happened offshore. Figure 12 shows the locations of the earthquakes with the different colours indicating the different countries.

The third dataset is the wine quality dataset³. The dataset contains 12 physicochemical features of red (1,599 observations) and white (4,898 observations) variants of the Portuguese "Vinho Verde" wine. For more details see Cortez et al. (2009). The fourth dataset refers to clients of a wholesale distributor⁴. It includes the annual spending in monetary units (m.u.) on 6 diverse product categories. The observations in both datasets were first normalized to become unitvectors.

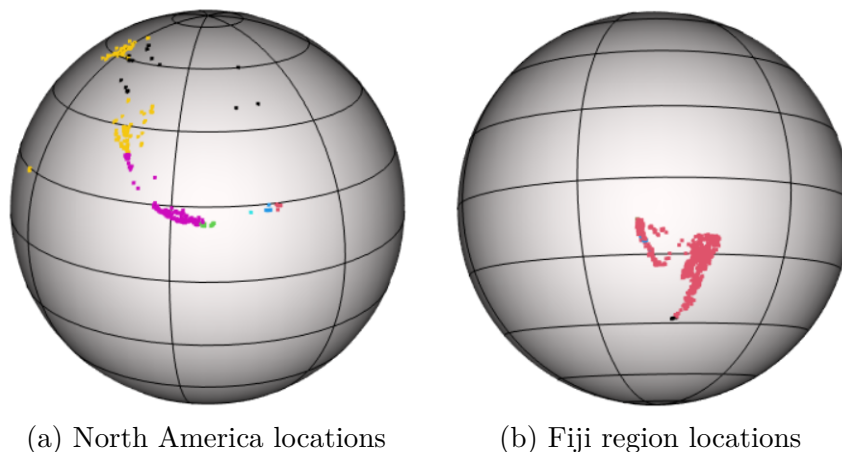


Figure 12: The locations of the earthquakes in North America and Fiji region.

¹This dataset was downloaded from <https://earthquake.usgs.gov>.

²This dataset constitutes a subsample from a larger dataset of containing 5,000 observations and is available by default in R by the names quakes.

³This dataset was downloaded from <https://archive.ics.uci.edu/dataset/186/wine+quality>.

⁴This dataset was downloaded from <https://archive.ics.uci.edu/dataset/292/wholesale+customers>.

5.1 North America

We searched for the optimal number of components K , using $K = 1, \dots, 6$. When fitting the SESPC, the search required 4.75 seconds, whereas the ESAG required 6.51 seconds. Figures 13(a)–13(b) present the ICL values for the mixtures of both distributions using the selected range of K , indicating that both mixtures agree that 4 clusters are enough. Figures 13(c)–13(d) visualize, on the sphere, the 4 clusters identified by each mixture of distributions. Evidently, the two distributions agree in the green and red clusters, but disagree in the black and blue clusters. Hawaii is clustered as red using the SESPC, where it is clustered as blue using the ESAG distribution. Notable differences also occur with some western and eastern USA locations, as indicated by the different colours. Note also that the SESPC mixtures have discriminated the locations almost perfectly, they are separable linearly whereas the ESAG mixtures have created overlapping clusters that are not linearly separable.

As an extra visualization of the results, we plotted the locations (latitude and longitude) in a 2D plot in Figures 13(e)–13(f). Distances in the 2D plot are not geodesic distances, two points that look far apart may be close on the sphere and vice versa. Since the clustering was done in 3D Cartesian space (or on the sphere directly), a visually comparison of the latitude/longitude coordinates can make a geometrically good clustering look bad and vice versa. For this reason we also projected the the data onto the first two principal components of the Cartesian coordinates. Figure 13(g)–13(h) shows the principal component analysis (PCA) projected data and the results are nearly the same, the 4 groups are nearly linearly separable using the SESPC mixtures.

We repeated the analysis creating a concomitant model, using the magnitude of the earthquakes as a covariate to link to the mixing probabilities. We did not attempt the mixture of regressions model simply because the magnitude is affected by the locations and not vice versa, but it seemed natural to affect the mixing probabilities. The results were nearly the same, the effect of the magnitude was shown to be rather weak.

5.2 Fiji region

Since Fiji region contains more locations, we searched for the optimal number of components K , using $K = 1, \dots, 10$. When fitting the SESPC, with parallel processing using 9 cores, the search required 69.98 seconds, whereas the ESAG required 110.83 seconds. Figures 14(a)–14(b) present the ICL values for the mixtures of both distributions using the selected range of K . The SESPC mixtures selected 49 clusters, whereas the ESAG mixtures was less parsimonious selecting 7 clusters. Figures 14(c)–14(d) visualize, on the sphere, the clusters identified by each mixture of distributions. Figure 14(e)–14(f) present the PCA projected data with colours identifying the different clusters. Looking at Figures 14(c)–14(f) we can observe that the SESPC mixtures created clusters that are easier to separate in comparison to the clusters created using the ESAG mixtures.

We used again the magnitude of the earthquakes as a covariate in the concomitant model. The BIC and ICL of the SESPC mixtures reduced significantly, yet the concomitant model selected 4 clusters and the groups were affected, but to a small degree. The magnitude had a significant impact on the ESAG mixtures, where this time 6 clusters were selected. Figure 15 displays the ICL for the ESAG concomitant model and the spherical plot of the data with the clusters in different colours.

5.3 Wine quality data

Figure 16(a) displays the data onto the sphere with the 2 groups in different colours. The SESPC and ESAG mixture models both correctly identified 2 clusters and their estimated clusters are displayed in Figures 16(c)–(d). The ESAG is shown to have identified the two clusters more properly and this is evident from the ARI values that were 0.546 and 0.700 for the SESPC and ESAG mixtures, respectively. The SC mixture model identified 13 clusters in the original data and 2 in the projected spherical data. However, the estimated clusters differ significantly as seen in Figure 16(b) and this was evident in the ARI value that was the lowest, only 0.476.

5.4 Wholesale data

Figure 17(a) displays the data onto the sphere with the 2 groups in different colours. The SC mixture model identified 14 clusters in the original data and 2 in the projected spherical data. Interestingly enough, the ESAG mixture model detected 3 clusters, whereas the SESPC model detected 2 clusters, as seen in Figures 17(c)–(d).

6 Conclusions

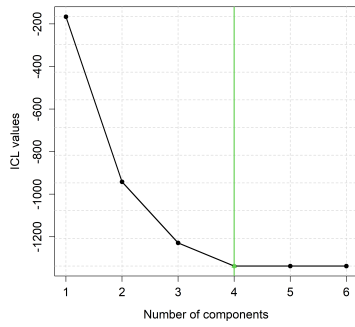
We proposed mixture models based on two elliptically symmetric distributions defined on the sphere for clustering spherical data. The benefit of these mixture models over rotationally symmetric distributions is that they escape the isotropic covariance matrix assumption and allow for a more general covariance matrix that produces ellipsoidal contours.

The simulation studies revealed that when the ground-truth model is the ESAG mixtures, both distributions perform equally well, but if the data are generated from a mixture of SESPC distributions, the SESPC mixture model outperforms the ESAG mixture model.

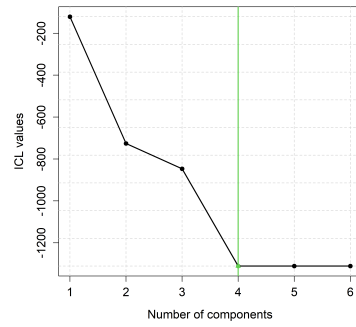
When applied to two real spherical data containing the locations of earthquakes the two mixture models identified the same number of components in North America, albeit clustering not the same locations. The clusters identified by the SESPC mixtures are easier to linearly separate than the ESAG mixtures. With Fiji region though, the SESPC mixtures identified 4 clusters, whereas the ESAG mixtures identified 7 clusters. The concomitant model made

no impact on the North America dataset, whereas for the Fiji region reduced the number of clusters identified by ESAG.

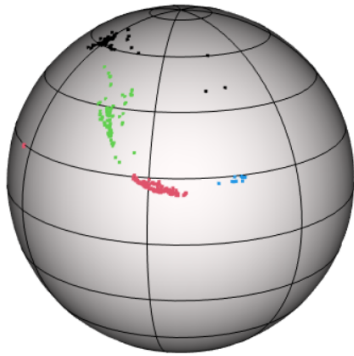
Since the two proposed models could not be applied directly to hyper-spherical data we projected them onto the sphere first. Based on the ARI criterion, the two elliptical symmetric distributions performed better than the rotational symmetric SC distribution.



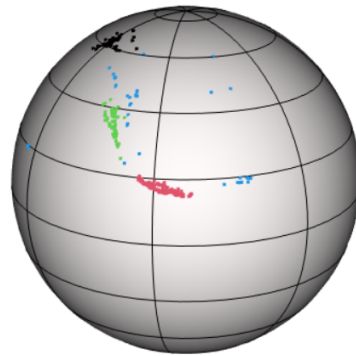
(a) ICL for SESPC mixtures



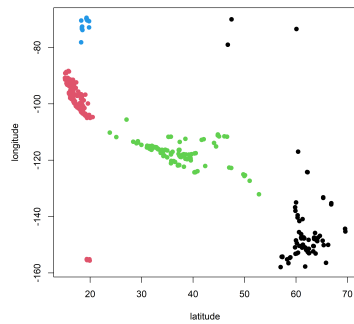
(b) ICL for ESAG mixtures



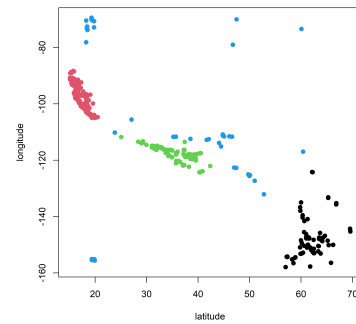
(c) Spherical plot of SESPC mixtures



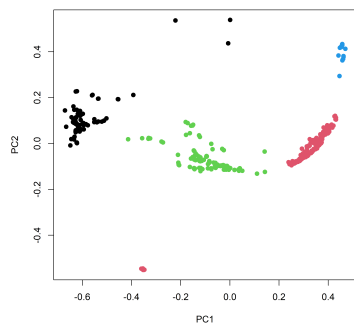
(d) Spherical plot of ESAG mixtures



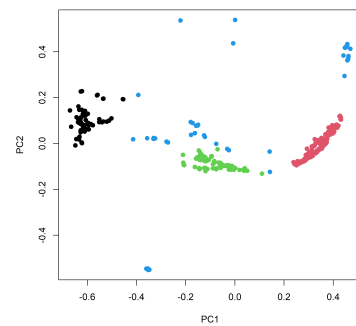
(e) 2D plot of SESPC mixtures



(f) 2D plot of of ESAG mixtures

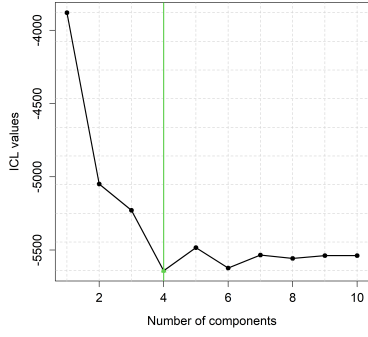


(g) PCA plot of SESPC mixtures

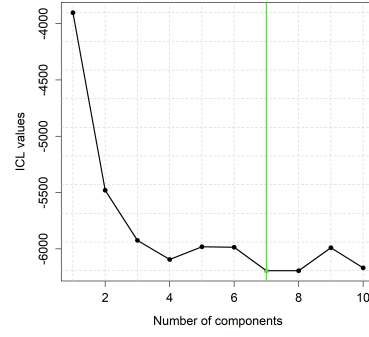


(h) PCA plot of of ESAG mixtures

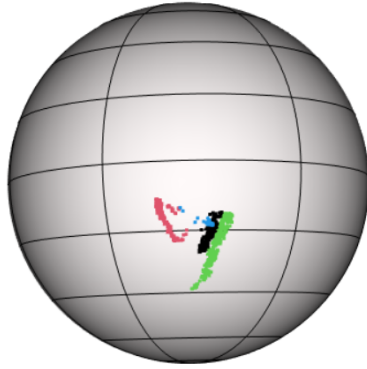
Figure 13: North America: ICL plots for the two mixtures and locations of the earthquakes coloured according to their estimated cluster.²³



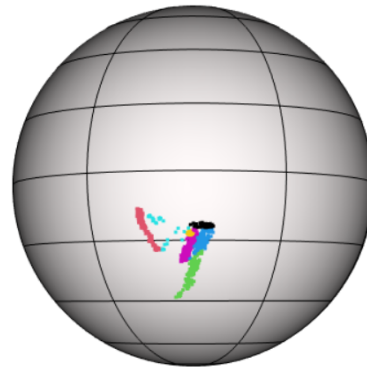
(a) ICL for SESPC mixtures



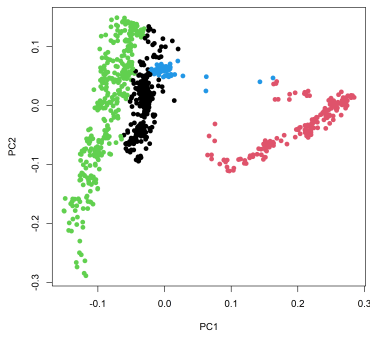
(b) ICL for ESAG mixtures



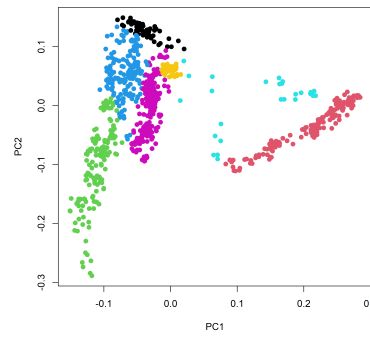
(c) Spherical plot of SESPC mixtures



(d) Spherical plot of ESAG mixtures



(e) PCA plot of SESPC mixtures



(f) PCA plot of of ESAG mixtures

Figure 14: Fiji region: ICL plots for the two mixtures and locations of the earthquakes coloured according to their estimated cluster.

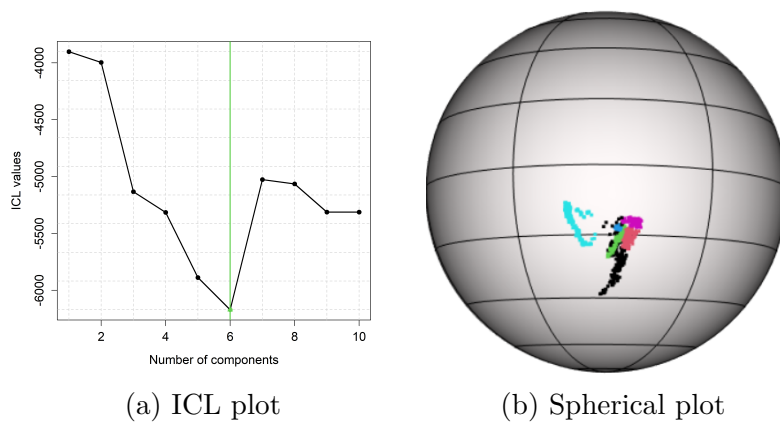


Figure 15: Fiji region: ICL and spherical plot for the ESAG concomitant model.

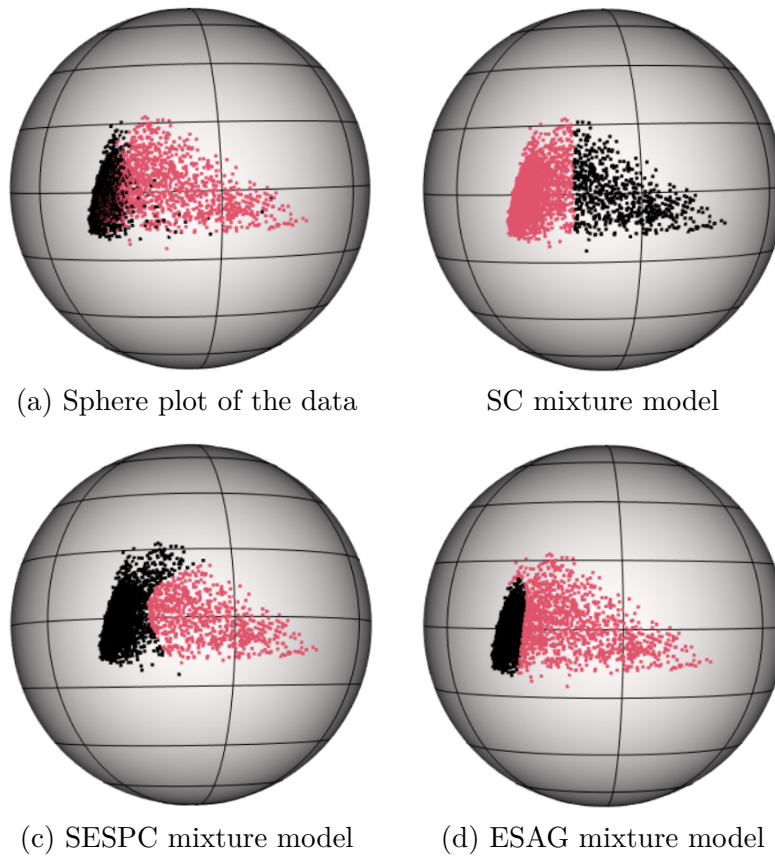


Figure 16: Wine quality data: Sphere plot of the data with the true groups in different colours and the results of the SESPC and ESAG mixture models.

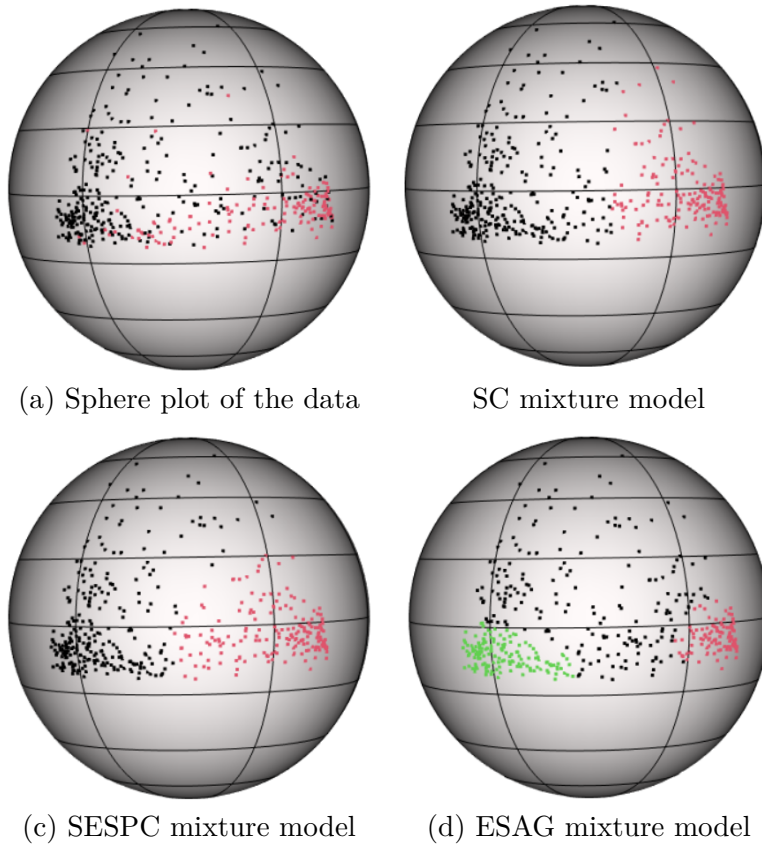


Figure 17: Wholesale data: Sphere plot of the data with the true groups in different colours and the results of the SESPC and ESAG mixture models.

References

- Banerjee, A., Dhillon, I. S., Ghosh, J., and Sra, S. (2005). Clustering on the unit hypersphere using von Mises–Fisher distributions. *Journal of Machine Learning Research*, 6:1345–1382.
- Barbaro, F. and Rossi, F. (2021). Sparse mixture of von Mises-Fisher distribution. In *ESANN 2021-European Symposium on Artificial Neural Networks, Computational Intelligence and Machine Learning*, pages 263–268. Ciaco-i6doc. com.
- Baudry, J.-P. and Celeux, G. (2015). EM for mixtures: Initialization requires special care. *Statistics and Computing*, 25:713–726.
- Biernacki, C., Celeux, G., and Govaert, G. (2000). Assessing a mixture model for clustering with the integrated completed likelihood. *IEEE Transactions on Pattern Analysis and Machine Intelligence*, 22(7):719–725.
- Biernacki, C., Celeux, G., and Govaert, G. (2003). Choosing starting values for the EM algorithm for getting the highest likelihood in multivariate Gaussian mixture models. *Computational Statistics & Data Analysis*, 41(3-4):561–575.
- Bullock, I. M., Feix, T., and Dollar, A. M. (2014). Analyzing human fingertip usage in dexterous precision manipulation: Implications for robotic finger design. In *2014 IEEE/RSJ International Conference on Intelligent Robots and Systems*, pages 1622–1628. IEEE.
- Chang, T. (1986). Spherical regression. *The Annals of Statistics*, 14(3):907–924.
- Cortez, P., Cerdeira, A., Almeida, F., Matos, T., and Reis, J. (2009). Modeling wine preferences by data mining from physicochemical properties. *Decision support systems*, 47(4):547–553.
- Dempster, A., Laird, N., and Rubin, D. (1977). Maximum Likelihood from Incomplete Data via the EM Algorithm. *Journal of the Royal Statistical Society, Series B*, 39(1):1–38.
- Dong, A. and Melnykov, V. (2024). Contaminated Kent mixture model for clustering non-spherical directional data with heavy tails or scatter. *Statistics & Probability Letters*, 208:110058.
- Fisher, R. A. (1953). Dispersion on a sphere. *Proceedings of the Royal Society of London. Series A. Mathematical and Physical Sciences*, 217(1130):295–305.
- Fletcher, P. T., Lu, C., Pizer, S. M., and Joshi, S. (2004). Principal geodesic analysis for the study of nonlinear statistics of shape. *IEEE transactions on medical imaging*, 23(8):995–1005.

- Fraley, C., Raftery, A., and Wehrens, R. (2005). Incremental model-based clustering for large datasets with small clusters. *Journal of Computational and Graphical Statistics*, 14(3):529–546.
- Fruhworth-Schnatter, S., Celeux, G., and Robert, C. P. (2019). *Handbook of mixture analysis*. Boca Raton: CRC press.
- Golzy, M. and Markatou, M. (2020). Poisson kernel-based clustering on the sphere: convergence properties, identifiability, and a method of sampling. *Journal of Computational and Graphical Statistics*, 29(4):758–770.
- Gopal, S. and Yang, Y. (2014). Von Mises–Fisher Clustering Models. In *International Conference on Machine Learning*, pages 154–162. PMLR.
- Heaton, M., Katzfuss, M., Berrett, C., and Nychka, D. (2014). Constructing valid spatial processes on the sphere using kernel convolutions. *Environmetrics*, 25(1):2–15.
- Hornik, K. and Grün, B. (2014). movMF: An R package for fitting mixtures of von Mises–Fisher distributions. *Journal of Statistical Software*, 58(10):1–31.
- Jung, S., Dryden, I. L., and Marron, J. S. (2012). Analysis of principal nested spheres. *Biometrika*, 99(3):551–568.
- Kagan, Y. Y. (2013). Double-couple earthquake source: symmetry and rotation. *Geophysical Journal International*, 194(2):1167–1179.
- Kagan, Y. Y. and Jackson, D. D. (2015). Likelihood analysis of earthquake focal mechanism distributions. *Geophysical Journal International*, 201(3):1409–1415.
- Karlis, D. and Xekalaki, E. (2003). Choosing initial values for the EM algorithm for finite mixtures. *Computational Statistics & Data Analysis*, 41(3-4):577–590.
- Kato, S. and McCullagh, P. (2020). Some properties of a Cauchy family on the sphere derived from the Möbius transformations. *Bernoulli*, 26(4):3224–3248.
- Kendall, D. G. (1974). Pole-seeking Brownian motion and bird navigation. *Journal of the Royal Statistical Society: Series B (Methodological)*, 36(3):365–402.
- Kent, J. T. (1982). The Fisher-Bingham distribution on the sphere. *Journal of the Royal Statistical Society: Series B (Methodological)*, 44(1):71–80.
- Kent, J. T., Hussein, I., and Jah, M. K. (2016). Directional distributions in tracking of space debris. In *2016 19th International Conference on Information Fusion (FUSION)*, pages 2081–2086. IEEE.

- Mardia, K. V. (1975). Statistics of directional data. *Journal of the Royal Statistical Society: Series B (Methodological)*, 37(3):349–371.
- McGraw, T., Vemuri, B. C., Yeziarski, B., and Mareci, T. (2006). Von Mises-Fisher mixture model of the diffusion ODF. In *3rd IEEE International Symposium on Biomedical Imaging: Nano to Macro, 2006.*, pages 65–68. IEEE.
- McLachlan, G. (2000). *Finite mixture models*. New York: John Wiley & Sons.
- McNicholas, P. D. (2016). *Mixture model-based classification*. Boca Raton: Chapman and Hall/CRC.
- Michael, S. and Melnykov, V. (2016). An effective strategy for initializing the EM algorithm in finite mixture models. *Advances in Data Analysis and Classification*, 10:563–583.
- Paine, P., Preston, S. P., Tsagris, M., and Wood, A. T. (2018). An elliptically symmetric angular Gaussian distribution. *Statistics and Computing*, 28(3):689–697.
- Papastamoulis, P., Martin-Magniette, M.-L., and Maugis-Rabusseau, C. (2016). On the estimation of mixtures of Poisson regression models with large number of components. *Computational Statistics & Data Analysis*, 93:97–106.
- Peel, D., Whiten, W. J., and McLachlan, G. J. (2001). Fitting mixtures of Kent distributions to aid in joint set identification. *Journal of the American Statistical Association*, 96(453):56–63.
- Røge, R. E., Madsen, K. H., Schmidt, M. N., and Mørup, M. (2017). Infinite von Mises–Fisher mixture modeling of whole brain fMRI data. *Neural Computation*, 29(10):2712–2741.
- Scealy, J. and Wood, A. T. (2019). Scaled von Mises–Fisher distributions and regression models for paleomagnetic directional data. *Journal of the American Statistical Association*.
- Straub, J., Chang, J., Freifeld, O., and Fisher III, J. (2015). A Dirichlet process mixture model for spherical data. In *Artificial Intelligence and Statistics*, pages 930–938. PMLR.
- Taghia, J., Ma, Z., and Leijon, A. (2014). Bayesian estimation of the von-Mises Fisher mixture model with variational inference. *IEEE transactions on pattern analysis and machine intelligence*, 36(9):1701–1715.
- Tsagris, M. and Alzeley, O. (2025). Circular and Spherical Projected Cauchy Distributions: A Novel Framework for Circular and Directional Data Modeling. *Australian & New Zealand Journal of Statistics*, 67(1):77–103.
- Tsagris, M., Papastamoulis, P., and Kato, S. (2025). Directional data analysis: spherical Cauchy or Poisson kernel-based distribution? *Statistics and Computing*, 35(2):51.

- Walsh, D., Arnold, R., and Townend, J. (2009). A Bayesian approach to determining and parametrizing earthquake focal mechanisms. *Geophysical Journal International*, 176(1):235–255.
- Yao, W. and Xiang, S. (2024). *Mixture Models: Parametric, Semiparametric, and New Directions*. Boca Raton: CRC Press.
- Zehao, Y. and Xianzheng, H. (2024). A new parameterization for elliptically symmetric angular Gaussian distributions of arbitrary dimensions. *Electronic Journal of Statistics*, 18(1):301–334.

Appendix

Choice of the parameters regarding the Hyper-sphere ESAG distribution

Since we are investigating a 10-variate ESAG distribution the vector γ consists of 44 values ($44 = 0.5(d^2 + d - 2)$). As a result, for each cluster, we consider the vectors γ_1, γ_2 by generating 44 random numbers from $N(0, 1)$ for each case. In Figure 19, the corresponding vectors γ_1, γ_2 are illustrated, for the three investigated cases presented in Figure 3. As for the choice of the mean vectors μ'_1, μ'_2 , they were derived similarly to the numerical analysis for Spherical data and are presented in Figure 18 using $(\tau_1, \tau_2) = (20, 20)$

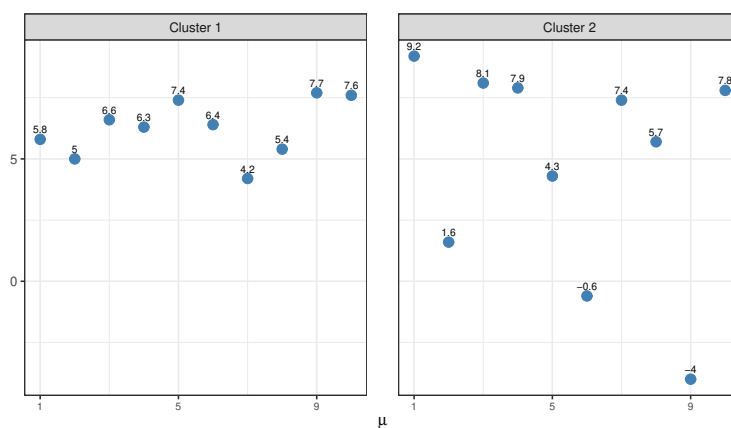
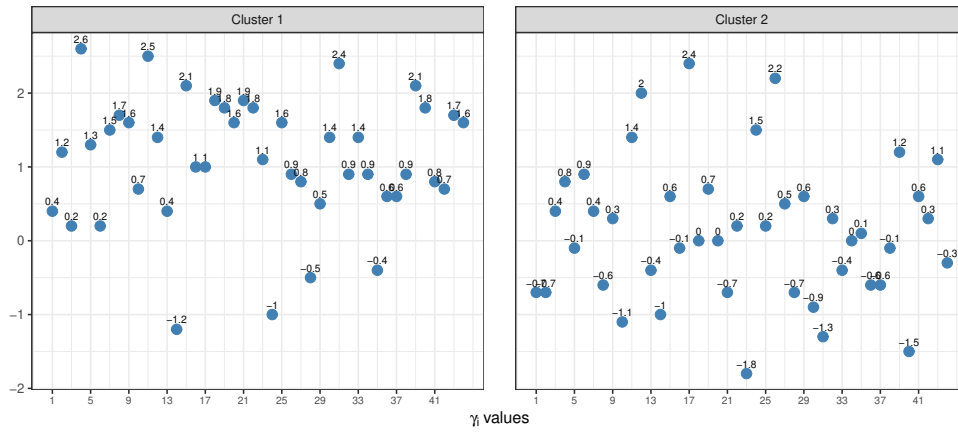
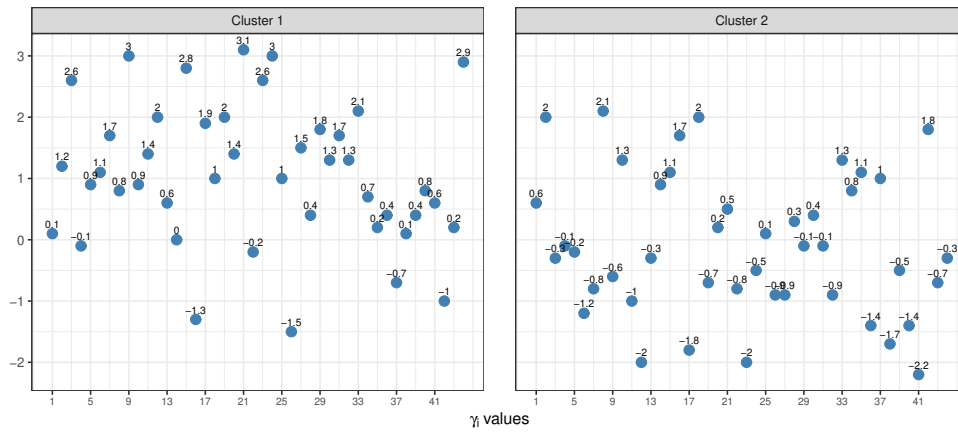


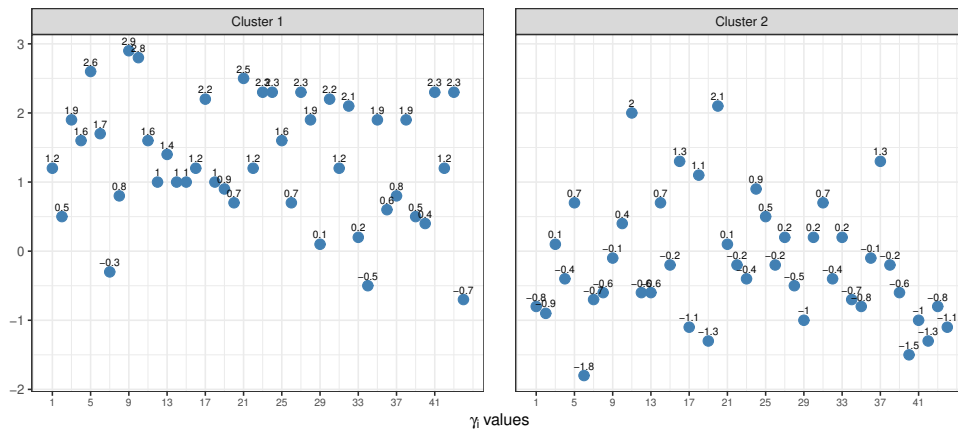
Figure 18: Values of μ'_1, μ'_2 using $(\tau_1, \tau_2) = (20, 20)$ for the 3 cases presented in Figure 3.



(a) Case 1



(b) Case 2



(c) Case 3

Figure 19: Values of γ_1 , γ_2 for the 3 cases presented in Figure 3.